



Supplement of

Convection-permitting climate model representation of severe convective wind gusts and future changes in southeastern Australia

Andrew Brown et al.

Correspondence to: Andrew Brown (andrewb1@student.unimelb.edu.au)

The copyright of individual parts of the supplement might differ from the article licence.

Contents

S1. Comparing wind gusts at 10-minute frequency using instantaneous versus maximum data	2
S2. Environmental diagnostics and clustering	3
S3. Daily maximum wind gust distribution for BARPAC-M historical climate simulation	6
S4. Wind gust ratio distribution for lightning-associated gusts	8
S5. Examples of simulated severe convective wind events	9
S6. Cluster-wise comparison of severe convection frequency, and related large-scale environments, between BARPAC-M and observations	12
S7. Spatial patterns of future changes	13

S1. Comparing the observed wind gust distribution at 10-minute frequency using instantaneous and maximum data

Observed wind gust data (main text Section 2.2) are used to investigate the sampling bias introduced when comparing instantaneous 10-minute BARPA-R gusts to 10-minute maximum gusts from observations and BARPAC-M. This is done using 11 years of observations (December–February months only) from an automatic weather station in south-east Australia (Melbourne Airport, 37.6654S, 144.8322E). The observed wind gust data are available as maxima over one-minute intervals, and are resampled to every 5 minutes to match the frequency of BARPA-R model time steps. Then, the 5-minute data is resampled to a 10-minute maximum and 10-minute instantaneous time series, to investigate the potential BARPA-R sampling bias. The 10-minute instantaneous and maximum distributions are then compared in Figure S1, showing a bias of around -1.0 m/s to -0.5 m/s using instantaneous data, for most of the distribution (up to the 99.99th percentile, with significant uncertainties for gusts stronger than that).

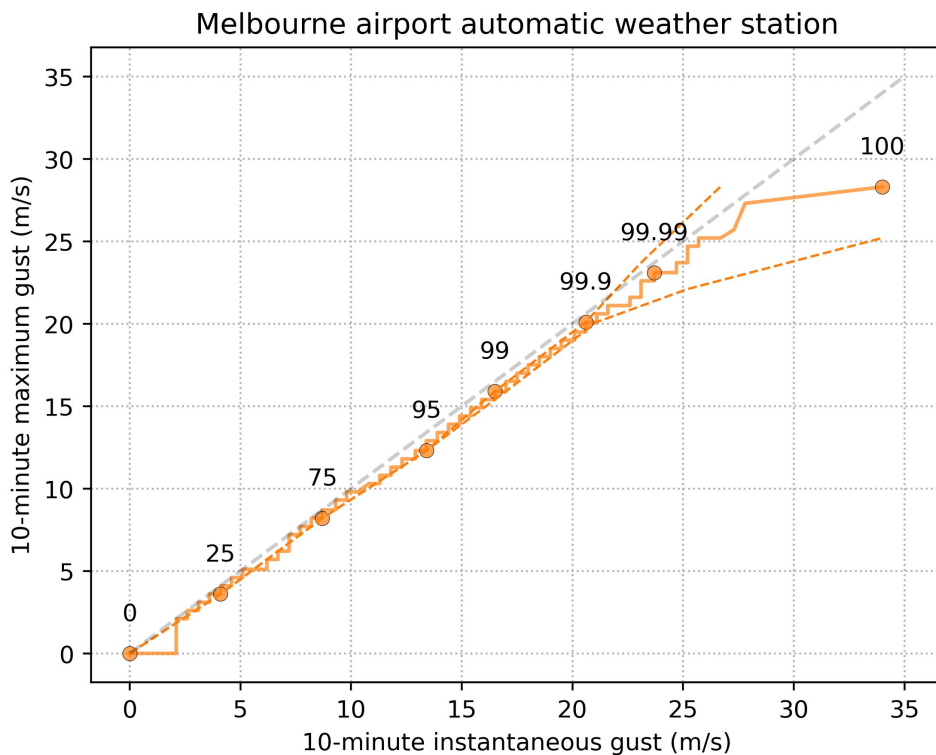


Figure S1: Quantile-quantile plot comparing the wind gust distribution at Melbourne Airport, based on observed data at 5-minute frequency using two resampling methods: 10-minute maximum and 10-minute instantaneous. The plot uses 1,000 evenly spaced percentiles up to the 95th, and then by plotting a number of percentiles equivalent to 5% of the number of samples from the 95th to 100th percentile. A selection of percentiles are also indicated with circle markers, and labelled with text. Dashed lines represents a two-sided 95% confidence interval calculated by resampling each distribution 1,000 times with replacement, and calculating each of the labelled percentiles

S2. Environmental diagnostics and clustering

We evaluate the representation of the environmental diagnostics relevant for BARPA-R, by comparing the distribution of six diagnostics with ERA5, across all available 6-hourly time steps and all AWS locations (see main text Figure 1). We also describe the severe convective wind (SCW) event clustering approach used in Sections 3.3 and 4 of the main text, developed by Brown et al. (2023) based on the large-scale environment, and investigate the representation of SCW clusters between ERA5 and BARPA-R. The diagnostics investigated here are the deep-layer mass-weighted mean wind speed from 0–6 km (U_{mean06} , m/s), deep-layer vertical wind shear (S_{06} , m/s), 0–1 km mean water vapour mixing ratio (Q_{mean01} , g/kg), 1–3 km temperature lapse rate (LR_{13} , K/km), convective available potential energy (CAPE, J/kg), and downdraft CAPE (DCAPE, J/kg).

U_{mean06} , S_{06} , LR_{13} , and S_{06} are investigated here given that they are used for the clustering of SCW events in Sections 3.3 and 4. This clustering has been defined based on 36 SCW cases in eastern Australia by Brown et al. (2023) using a k-means approach, with those cluster centroids applied directly here resulting in strong background wind, steep lapse rate, and high moisture types of SCW events. Following Brown et al. (2023), this clustering is visualised in Figure S2, based on joint distributions of the four variables mentioned above. These distributions are calculated from ERA5 based on observed SCW events, and from BARPA-R based on SCW events simulated by BARPAC-M (see Section 3.2 of the main text for definition of observed and simulated SCW events). Figure S2 demonstrates that the distribution of those variables in each SCW cluster is similar between ERA5 and BARPA-R, giving some confidence in the application of this clustering method to the BARPA dataset. Although, there is less spread in the BARPA-R distribution across SCW events for U_{mean06} and LR_{13} , and there are many more steep lapse rate SCW events simulated by BARPAC-M compared with observations (see Section 3.3 of the main text for further details on this latter point).

The distribution of CAPE and DCAPE will also be investigated here between ERA5 and BARPA, given that these variables are important environmental controls for deep moist convection and strong downdrafts driven by the evaporation of precipitation. CAPE and DCAPE are both calculated using a combination of pressure level and surface level output in ERA5 and BARPA-R. For CAPE, all levels at or below 100 hPa are used (28 levels in ERA5 and 13 levels in BARPA-R), with the maximum CAPE in the column based on all possible starting parcels used here, noting that a virtual temperature correction is applied in the calculation. For DCAPE, the parcel with the lowest equivalent potential temperature between the surface and 400 hPa above ground level is used in the calculation.

Figure S3 shows the distributions of all diagnostics from BARPA-R and ERA5 for all available 6-hourly time steps in the analysis period, indicating good overall agreement between the two datasets, and providing confidence in the use of these diagnostics from BARPA-R. However, although there is good agreement here, these datasets are likely biased relative to other more accurate sources of the vertical atmospheric profile, such as radiosonde measurements (Taszarek et al., 2020). Some differences between ERA5 and BARPA-R are worth noting here, such as higher median and upper quartile values of Q_{mean01} in BARPA-R, as well as a longer tail of CAPE values, while the shape of the DCAPE distribution appears different towards the median and lower tail in each dataset (although quartile values agree very well). These differences could be due to a combination of increased horizontal resolution, differences in the number of vertical levels used to calculate the diagnostics, and model biases in the vertical profile of temperature and moisture.

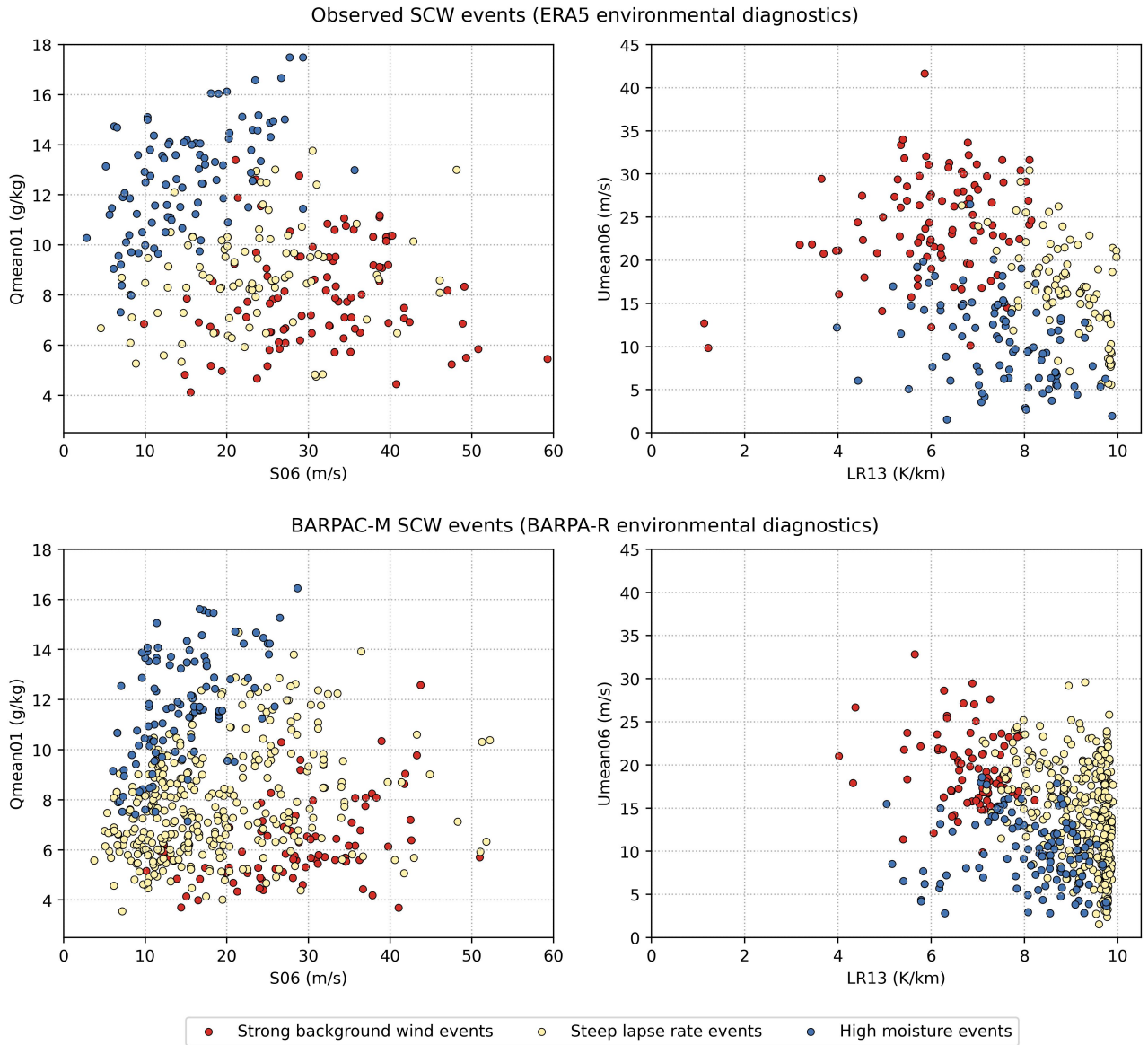


Figure S2: Joint distributions of (left column) the mean water vapour mixing ratio in the lowest 1 km (Q_{mean01}) and vertical wind shear between the surface and 6 km (S_{06}), as well as (right column) the temperature lapse rate between 1 and 3 km (LR_{13}) and the mass-weighted mean wind speed from the surface to 6 km (U_{mean06}), for severe convective wind (SCW) events from (top row) observations and (bottom row) BARPAC-M. For observed SCW events, the environmental diagnostics shown here are calculated from ERA5, while for BARPAC-M events, the diagnostics are calculated from BARPA-R. The joint distributions are separated based on the clustering method of Brown et al. (2023), including (red) strong background wind, (yellow) steep lapse rate, and (blue) high moisture SCW events.

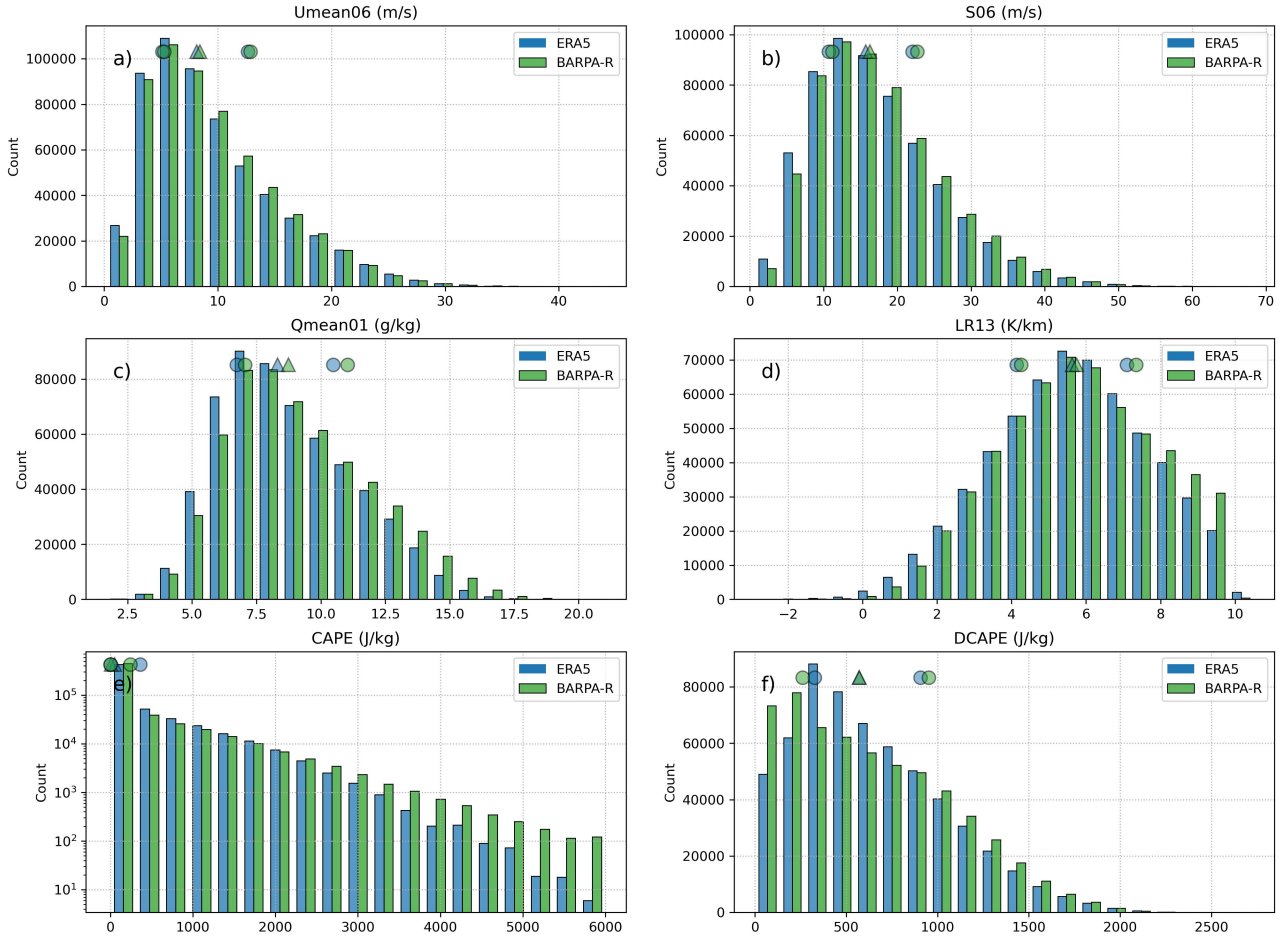


Figure S3: Histograms comparing the distribution of various diagnostics related to the convective environment between (blue) ERA5 and (green) BARPA-R, using all 6-hourly time steps at all AWS locations. This includes comparisons for (a) the mass-weighted mean wind speed from the surface to 6 km (Umean06), (b) vertical wind shear between the surface and 6 km (S06), (c) the mean water vapour mixing ratio in the lowest 1 km (Qmean01), (d) temperature lapse rate between 1 and 3 km (LR13), (e) convective available potential energy (CAPE), and (f) downdraft CAPE (DCAPE). Triangles in each panel represent the median of each distribution, while circles represent the upper and lower quartiles. Note that CAPE bin counts in panel (e) are shown with a log scale.

S3. Daily maximum wind gust distribution for BARPAC-M historical climate simulation

Daily maximum wind gust distributions are compared between the BARPAC-M hindcast and BARPAC-M historical climate simulation, over a 1990-2005 December–February period. Daily maximum wind gusts are taken from BARPAC-M output at the same AWS locations as shown in Figure 1 of the main text, using all 10-minute intervals over the period. As noted in the main text (Section 3.1 therein), the distributions are broadly similar compared with differences with BARPA-R and ERA-Interim gust data, although with a positive bias in the ACCESS-forced BARPAC-M distribution compared with the ERA-forced hindcast distribution (Figure S4). For comparison, the daily maximum distribution from the BARPAC-M hindcast over the 2005–2015 period (same as used in Figures 2a and b of the main text) is also shown on Figure S4, again constructed using all 10-minute intervals over the period at all station locations. The distribution for the 2005–2015 period is shifted to slightly higher values compared with the 1990–2005 period, demonstrating potential long-term variability in the wind gust distribution as simulated by BARPAC-M.

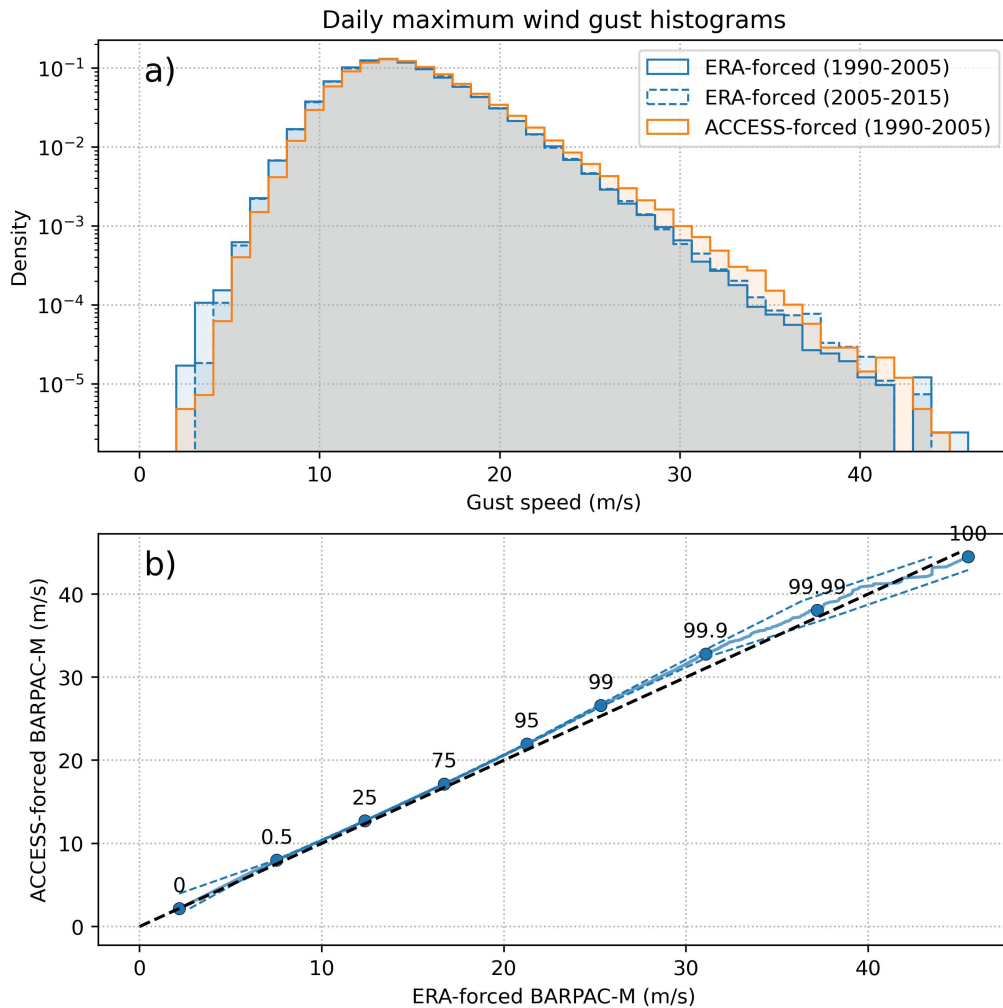


Figure S4: a) Daily maximum wind gust distribution for (blue solid line) BARPAC-M hindcast over a 1990–2005 December–February period, and (orange solid line) BARPAC-M historical climate simulation over the same period. For comparison, the distribution for BARPAC-M forced by ERA-Interim over the same 2005–2015 period as used in Figure 2 of the main text is also shown with a blue dashed line. b) Quantile-quantile plot comparing the daily maximum wind gust distribution between the BARPAC-M hindcast (ERA-forced) and historical climate simulations (ACCESS-forced), with 95% confidence interval shown by dashed lines, generated by randomly resampling each distribution 1,000 times, with replacement.

S4. Wind gust ratio distribution for lightning-associated gusts

Here, severe ($25+$ m/s) daily maximum wind gusts from observations and BARPAC-M are associated with nearby deep convection by using lightning occurrence as a proxy. Specifically, a gust is classed as lightning-associated if at least one stroke is detected within 50 km of a AWS location on the day the gust occurred (and is non lightning-associated otherwise). For both BARPA models, the BARPAC-M parameterised lightning field is used for this, while WWLLN is used for gusts measured by AWS. It is noted that there is a higher frequency of lightning occurrence produced by BARPAC-M compared with WWLLN, related to many more total lightning flashes in BARPAC-M compared with WWLLN (not shown). This could be related to biases in the BARPA model, although WWLLN is not intended to detect all lightning flashes, especially intra-cloud flashes, and so is likely low-biased relative to the actual number of flashes.

Figure S5 reveals that the wind gust ratio tends to be higher for observed severe daily maximum lightning-associated wind gusts, compared with severe daily maximum gusts that aren't associated with lightning. This is consistent with the understanding that severe wind gusts associated with convective processes are relatively strong and short-lived compared with gusts driven by synoptic-scale processes, with lightning used here as a proxy for deep convection. Similar behaviour is seen in the BARPAC-M dataset, suggesting that a significant proportion of BARPAC-M daily maximum gusts associated with lightning are also driven by convective processes as represented by the model. A wind gust ratio of 1.5 appears to be a good discriminator for lightning and non lightning-associated gusts, supporting its use for identifying severe convective wind events in the main text.

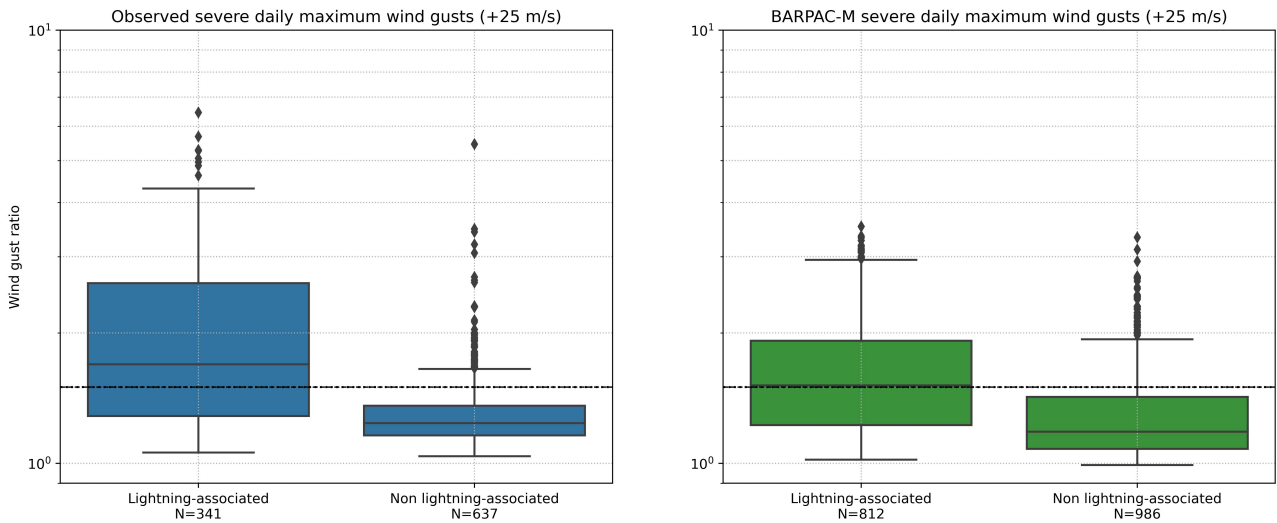


Figure S5: Boxplots of wind gust ratios for severe ($25+$ m/s), daily maximum wind gusts, for lightning and non lightning-associated wind gusts. Shown separately for (left) observations and (right) BARPAC-M. Boxes range from the 25th to the 75th percentile, with whiskers extending to 1.5 times the inter-quartile range, outliers shown with diamond markers, and the median represented by a horizontal line. The number of daily maximum gusts in each distribution (N) is indicated at the bottom of the figure. A wind gust ratio of 1.5, used for the definition of severe convective gusts in the main text, is indicated with a horizontal dashed line. Note that a logarithmic scale is used on the vertical axis.

S5. Examples of simulated severe convective wind events

To check that the severe convective wind gusts in BARPAC-M appear consistent with physical understanding, we compare the simulated spatial gust distribution and wind gust time series with observations, for two different events. Note that because it is difficult to observe the spatial gust distribution in reality, the BARPAC-M distribution will be compared with spatial patterns of observed radar reflectivity, given that the size and number of convective cells observed by radar should broadly correspond with the patterns of strong convective outflow that leads to severe winds. Because storm initiation and structure can look very different between the model and observations for a given day (noting there is no data assimilation in BARPAC-M), we use an analogue approach to analyse individual events. That is, we choose two of the highest intensity convective gust events from BARPAC-M that appear similar to events in the observational dataset in terms of the large-scale convective environment and synoptic conditions, and analyse the BARPAC-M gust characteristics for these events. Events are manually chosen from BARPAC-M based on being above the 99.99th percentile (43.2 m/s and 39.4 m/s), while still having different synoptic conditions to each other, however both occur in steep lapse rate environments (see Section 3.3 of the main text for more information regarding steep lapse rate environments). Both events are from the south-eastern part of the domain, one near the city of Melbourne (Figure S6) and one inland and to the west of Melbourne (Figure S7). We therefore use radar data from the Melbourne radar for comparisons, available in the Australian Unified Radar Archive (Soderholm et al., 2022). Note that the corresponding analogous events from observations occur at similar locations.

Figure S6 shows a severe convective wind gust event from BARPAC-M compared with an analogous observed event. Both events occur with moderate amounts of convective available potential energy (CAPE), and a deep layer of westerly winds with some turning of wind direction at low levels. The observed storm cells in this case were supercell storms (Allen, 2012), however we are unable to diagnose the BARPAC-M storm morphology here due to a lack of available data. BARPAC-M is shown here to produce a very similar gust time series to the analogous event, with spatial gust footprints consistent with the size of the storm cells in the observed event. A drop in temperature of around 3 degrees is also seen in the BARPAC-M time series, with the arrival of the gusty convective cold pool. Although it is difficult to compare with observations, the number of strong gust footprints in BARPAC-M appears potentially too high. The large amount of strong outflow regions is more noticeable in an animation of the BARPAC-M event, available here: <https://doi.org/10.26188/22767677.v1>. In addition, BARPAC-M has very warm surface temperatures and a deep dry adiabatic layer from the surface to nearly 600 hPa, that would promote strong downdrafts and outflow, contributing to much stronger wind gusts than the analogous observed case.

The BARPAC-M event in Figure S7 again has a deep dry adiabatic layer extending to nearly 500 hPa, with a similar, shallower layer present in the analogous observed event based on ERA5 (although the ERA5 temperature profile is sub dry-adiabatic near the surface). Both the BARPAC-M and observed event occurred in an environment with strong north-westerly flow through a deep layer, turning westerly at upper levels, with low values of CAPE. The observed wind gusts from cellular storms on this day were diagnosed as dry microbursts (Bureau of Meteorology, 2020). Again, the wind gust time series associated with the convective cells in BARPAC-M is very similar to the analogous observed event. In addition, the spatial gust footprints in BARPAC-M appear to be a similar size to the observed convective cells from radar. An animation for this BARPAC-M event can be seen here: <https://doi.org/10.26188/22767677.v1>. For both example events

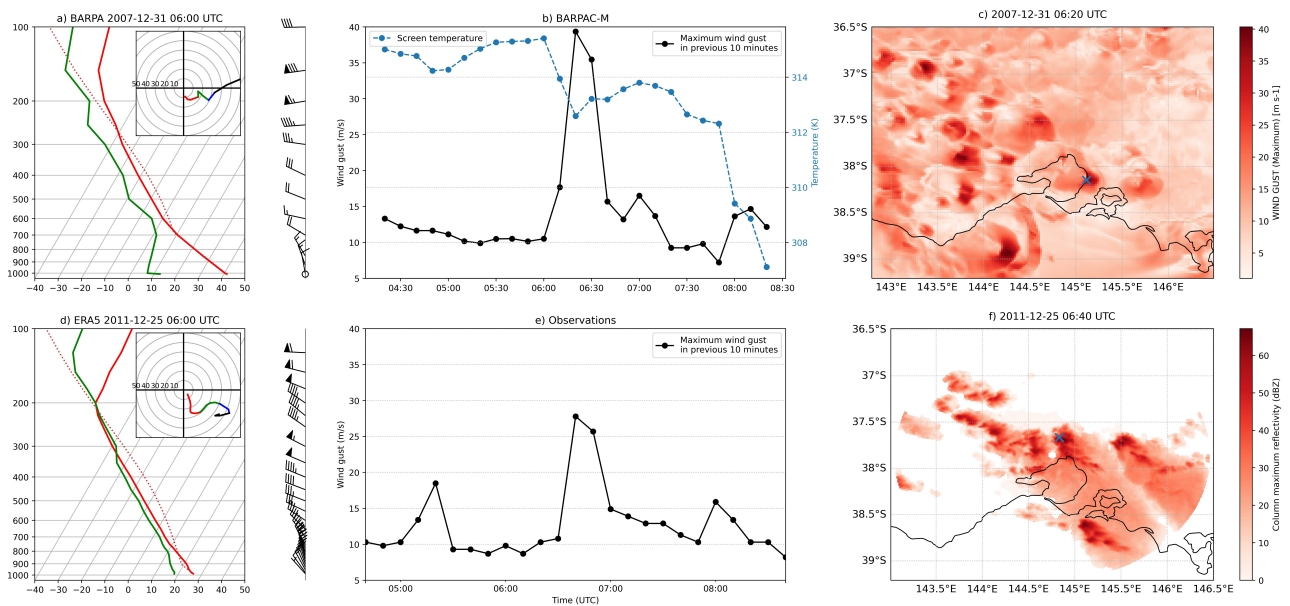


Figure S6: Example of a simulated severe convective wind event from BARPAC-M. Shown in terms of (a) associated sounding from BARPA-R, (b) the wind gust intensity and screen temperature time series, and (c) the spatial wind gust intensity distribution at the time of the maximum gust. The location of the gust time series is shown with a blue cross in (c). An analogous event from the observational record is also shown, in terms of (d) the associated sounding from ERA5, (e) the wind gust time series and (f) column maximum radar reflectivity. Sounding plots were made with the sharppy Python package (Blumberg et al., 2017). An animated version of this figure is available here: https://figshare.unimelb.edu.au/articles/figure/Two_examples_of_BARPAC-M_simulations_of_severe_wind_gusts_associated_with_convection_/22767677/1?file=40452371

examined here, BARPA-R does not reproduce the strong gust patterns due to having parameterised convection (see comparison animation here: <https://doi.org/10.26188/22767677.v1>).

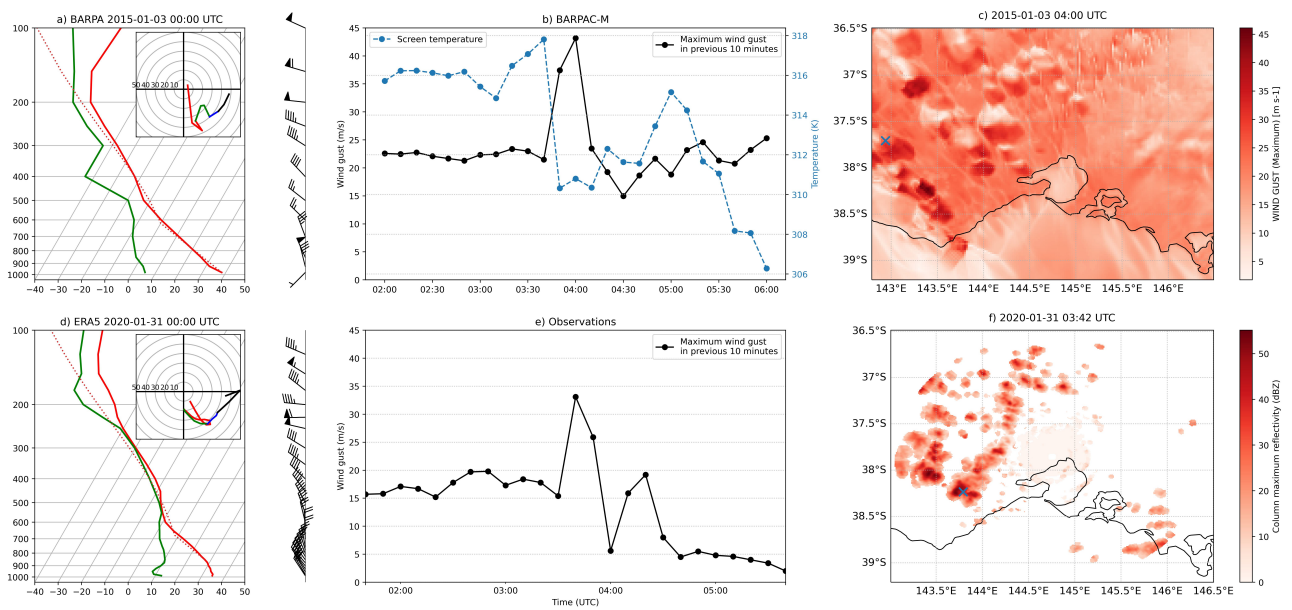


Figure S7: As in Figure S6 but for a different event from BARPAC-M. An animated version of this figure is available here: https://figshare.unimelb.edu.au/articles/figure/Two_examples_of_BARPAC-M_simulations_of_severe_wind_gusts_associated_with_convection_/22767677/1?file=40452368

S6. Cluster-wise comparison of lightning occurrence frequency and severe convective wind environments, between BARPAC-M and observations

Figure S8 shows that there is a similar frequency of occurrence for different types of SCW environmental clusters between BARPA-R and ERA5 (see Section 3.3 of the main text for more information regarding these clusters). There is also a similar frequency of large-scale environments that are favourable for SCWs between BARPA-R and ERA5, as diagnosed by the statistical diagnostic of Brown and Dowdy (2021b) (further details on this diagnostic are provided in Section 2.3 of the main text). In addition, there is a similar frequency of daily lightning occurrence between BARPAC-M and WWLLN for steep lapse rate environments. The results here indicate that the frequency of occurrence for large scale conditions favourable for SCWs is realistic in the BARPAC-M hindcast simulation, as is the frequency of severe convection as represented by lightning occurrence frequency. However, the frequency of SCW events produced in steep lapse rate environments is far too high (Figure S8c).

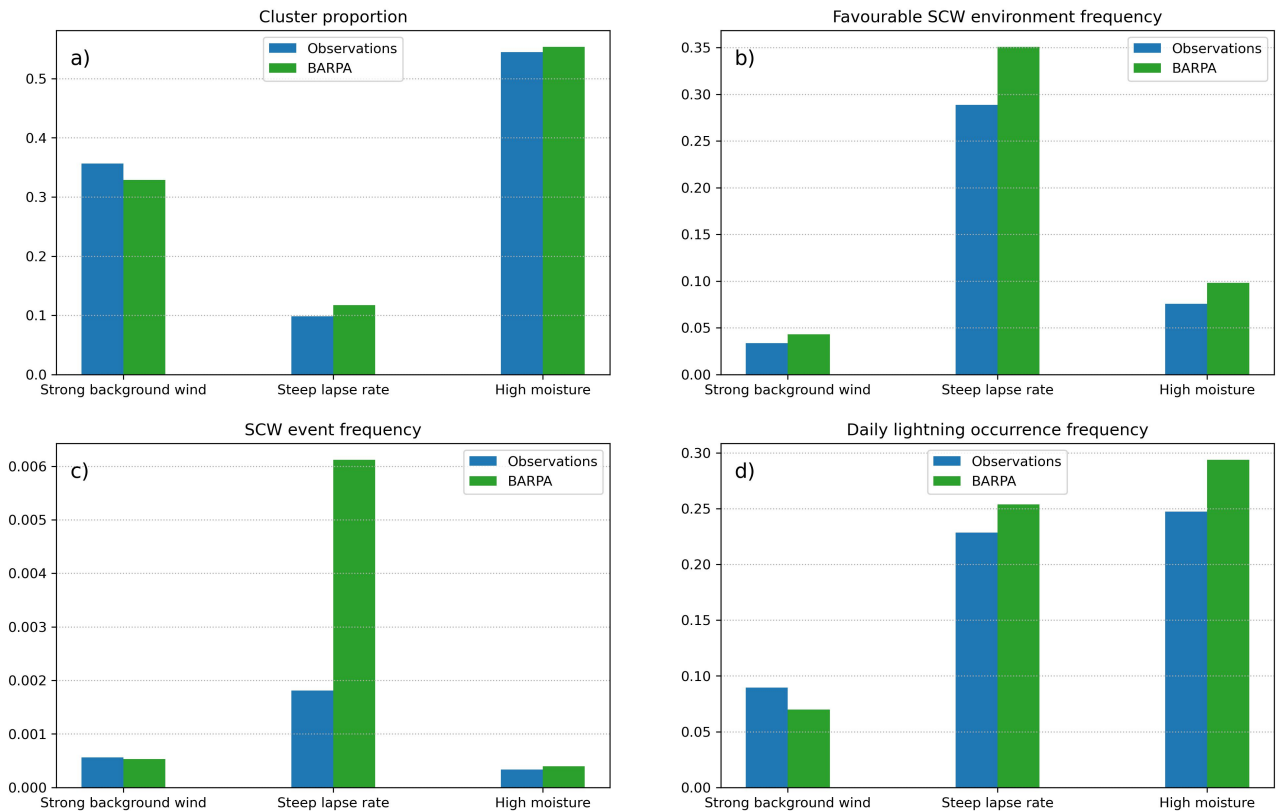


Figure S8: a) Frequency of each type of severe convective wind environment cluster from 6-hourly environmental data at all AWS locations and time steps. Shown separately for (blue) ERA5 (labelled "observations") and (green) BARPA-R (as used for clustering of BARPAC-M wind gusts). b) As in (a) but for the frequency of a favourable severe convective wind environment, following the method of Brown and Dowdy (2021a). c) As in (a) but for severe convective wind occurrence frequency from AWS (blue, "observations") and BARPAC-M (green). d) Frequency of lightning occurrence within 50 km from daily data for each environmental cluster, shown for (blue) ERA5 and WWLLN (labelled "observations") and (green) BARPAC-M.

S7. Spatial patterns of future changes

Future changes in simulated SCWs and favourable SCW environments (F_ENV) are shown spatially for each event type, in terms of both daily probabilities and probabilities conditional on the occurrence of each environmental cluster (Figure S10). Base state probabilities for the historical period are also shown (Figure S9).

Similar to Figure 6 of the main text, Figure S9 shows that simulated SCWs occur in the south part of the domain in strong background wind environments, and in the northern/eastern part of the domain in high moisture environments. Simulated SCWs in steep lapse rate environments have relatively high probabilities, that occur over non-coastal regions throughout the domain. Conditional probabilities have a similar spatial distribution to non-conditional probabilities. The spatial distribution of favourable environment probabilities are similar to the simulated SCW distribution for the high moisture cluster. For strong background wind environments, favourable environment probabilities are also maximised in the southern part of the domain, but extend further up the east coast topography than the simulated SCW probabilities. Probabilities for favourable steep lapse rate environments are maximised along the south-east and east part of the domain, in contrast to the simulated SCW distribution for that cluster. Again, conditional probabilities for favourable environments are similar to non-conditional probabilities for each cluster.

Future changes in favourable environmental conditions are relatively consistent spatially, while changes in simulated SCWs are highly spatially variable, especially for the steep lapse rate cluster (Figure S10). Changes in overall F_ENV probabilities show significant regional variations, with increases inland and slight decreases or no change along the coastlines (Figure S10b).

Finally, the climatology and future change in the extreme upper tail of the simulated wind gust distribution is demonstrated spatially, using the 20-year convective wind gust maximum from the historical and mid-century BARPAC-M simulation (Figure S11). Although future increases are indicated in a large region throughout the central and southeastern part of the domain, many of these events in the future period occur on the same day within a broad region of convection (not shown). As a result, future changes in the upper-tail of the wind gust distribution across the domain are not statistically distinct from zero (main text, Figure 8).

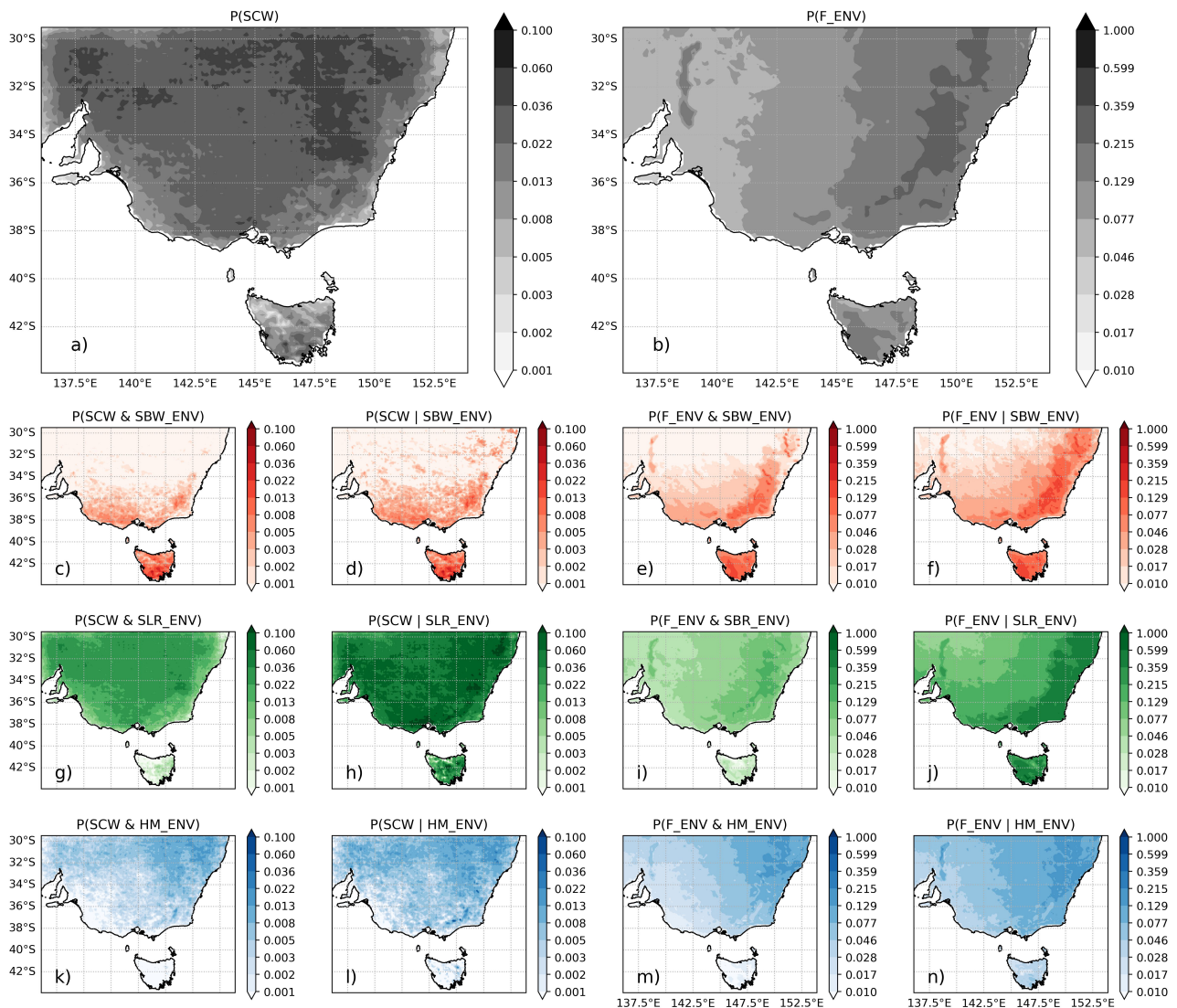


Figure S9: (a) Daily December–February probability of a simulated severe convective wind (SCW) event from the BARPAC-M historical climate simulation, on the same 0.11-degree grid as BARPA-R. (b) Daily December–February probability of a favourable severe convective wind environment (F_ENV), based on the statistical diagnostic of Brown and Dowdy (2021b) from the BARPA-R historical climate simulation. (c, g, k) As in (a), but for SCWs in strong background wind (SBW), steep lapse rate (SLR), and high moisture (HM) environments. (d, h, l) as in (c, g, k) but for daily SCW probabilities conditional on daily occurrences of each environmental cluster. (e, i, m) As in (c, g, k) but for F_ENV. (f, j, n) As in (d, h, l) but for F_ENV.

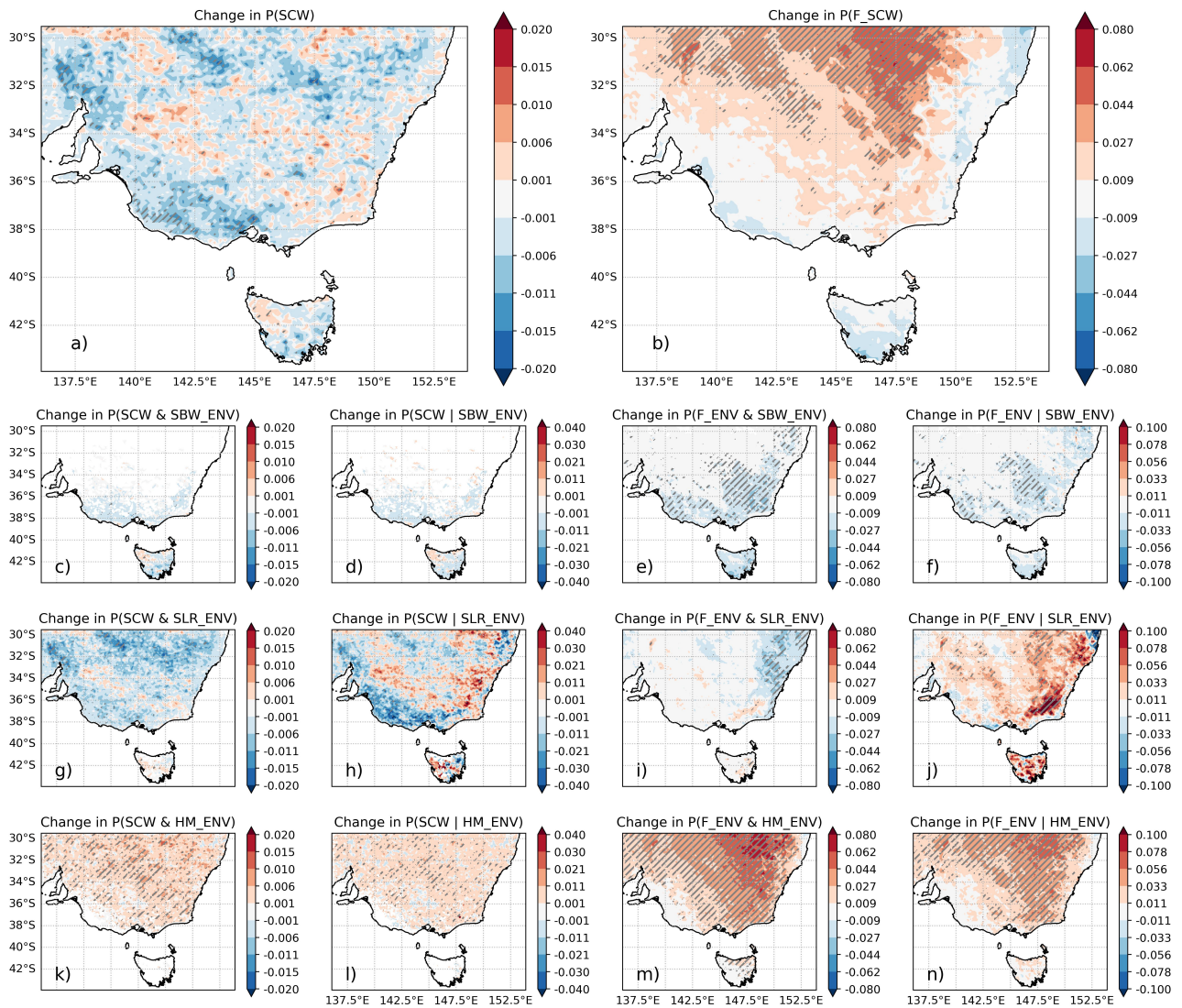


Figure S10: As in Figure S9, but showing absolute difference in daily probabilities between the historical BARPA simulations and mid-century simulations forced by ACCESS1-0 under a RCP8.5 scenario. Hatching represents changes that exceed a two-sided 95% confidence limit, based on randomly resampling monthly time blocks from the historical and future period, 1,000 times with replacement.

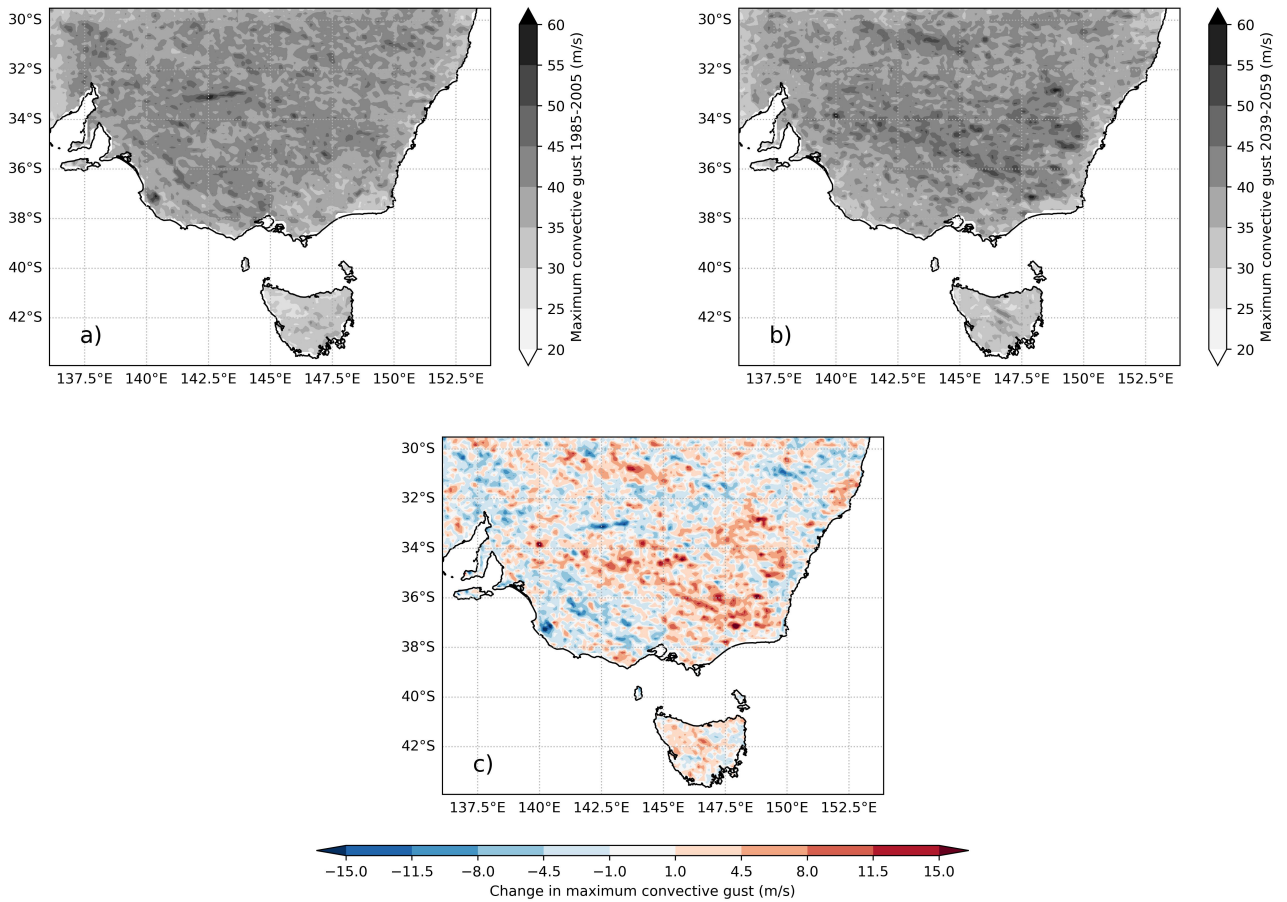


Figure S11: a) Maximum convective wind gust over a 20-year December–February (DJF) period from the BARPAC-M historical climate simulation. (b) As in (a), but for the mid-century climate simulation. (c) Change in maximum convective wind gust from the BARPAC-M model between the historical and mid-century period.

References

- Allen, J. T.: Supercell Storms: Melbourne’s white Christmas 2011, *Bulletin of the Australian Meteorological and Oceanographic Society*, 25, 47–51, 2012.
- Blumberg, W. G., Halbert, K. T., Supinie, T. A., Marsh, P. T., Thompson, R. L., and Hart, J. A.: Sharppy: An open-source sounding analysis toolkit for the atmospheric sciences, *Bulletin of the American Meteorological Society*, 98, 1625–1636, <https://doi.org/10.1175/BAMS-D-15-00309.1>, 2017.
- Brown, A. and Dowdy, A.: Severe Convective Wind Environments and Future Projected Changes in Australia, *Journal of Geophysical Research: Atmospheres*, 126, 1–17, <https://doi.org/10.1029/2021JD034633>, 2021a.
- Brown, A. and Dowdy, A.: Severe convection-related winds in Australia and their associated environments, *Journal of Southern Hemisphere Earth System Science*, <https://doi.org/10.1071/ES19052>, 2021b.
- Brown, A., Dowdy, A., Lane, T. P., and Hitchcock, S.: Types of Severe Convective Wind Events in Eastern Australia, *Monthly Weather Review*, 151, 419–448, <https://doi.org/10.1175/MWR-D-22-0096.1>, 2023.
- Bureau of Meteorology: Report into the meteorological aspects of severe thunderstorm impacts near Cressy, Victoria on 31st January 2020. Attachment 3 in: ”Cost pass through application – 500kV Transmission Line Tower Collapse”, AusNet Services, Tech. rep., 2020.
- Soderholm, J., Louf, V., Brook, J., and Protat, A.: Australian Operational Weather Radar Level 1b Dataset, <https://doi.org/10.25914/40KE-NM05>, 2022.
- Taszarek, M., Pilguy, N., Allen, J. T., Gensini, V., Brooks, H. E., and Szuster, P.: Comparison of convective parameters derived from ERA5 and MERRA2 with rawinsonde data over Europe and North America, *Journal of Climate*, pp. 1–55, <https://doi.org/10.1175/JCLI-D-20-0484.1>, 2020.